

ARTICLE OPEN



Strong and tunable spin–orbit interaction in a single crystalline InSb nanosheet

Yuanjie Chen¹, Shaoyun Huang¹, Dong Pan^{1,2,3}, Jianhong Xue¹, Li Zhang¹, Jianhua Zhao^{2,3}✉ and H. Q. Xu^{1,3}✉

A dual-gate InSb nanosheet field-effect device is realized and is used to investigate the physical origin and the controllability of the spin–orbit interaction in a narrow bandgap semiconductor InSb nanosheet. We demonstrate that by applying a voltage over the dual gate, efficiently tuning of the spin–orbit interaction in the InSb nanosheet can be achieved. We also find the presence of an intrinsic spin–orbit interaction in the InSb nanosheet at zero dual-gate voltage and identify its physical origin as a build-in asymmetry in the device layer structure. Having a strong and controllable spin–orbit interaction in an InSb nanosheet could simplify the design and realization of spintronic devices, spin-based quantum devices, and topological quantum devices.

npj 2D Materials and Applications (2021)5:3; <https://doi.org/10.1038/s41699-020-00184-y>

INTRODUCTION

Low-dimensional narrow bandgap InSb nanostructures, such as nanowires and quantum wells, have in recent years attracted great interests. Due to their small electron effective mass, strong spin–orbit interaction (SOI), and large Landé g -factor, these nanostructures have potential applications in high-speed electronics¹, infrared optoelectronics², spintronics³, quantum electronics^{4,5} and topological quantum computation⁶. The past decade has witnessed booming investigations of devices made from epitaxially grown InSb nanowires, including field-effect transistors^{7,8}, single^{9–11} and double quantum dots^{12,13}, and semiconductor–superconductor hybrid quantum devices^{14–17}. Among the most influential, pioneer developments are the topological superconducting quantum devices made from InSb nanowires^{14,16}, in which zero-energy modes, a signature of Majorana fermions^{18,19} in solid state, were detected and studied. However, to build a device in which braiding of topological quantum states, such as Majorana fermions, can be conveniently performed and thus topological quantum computations can be designed and realized, it could be inevitable to move from single-nanowire structures to multiple-nanowire^{20,21} and two-dimensional (2D) planar quantum structures^{22–24}. Recently, high-quality InSb/InAlSb heterostructured quantum wells^{25,26} and free-standing InSb nanosheets^{27–30} have been achieved by epitaxial growth techniques. In comparison with InSb/InAlSb quantum well systems, the free-standing InSb nanosheets have advantages in direct contact by metals, including superconducting materials, in easy transfer to different substrates, and in convenient fabrication of dual-gate structures. With use of free-standing InSb nanosheets, lateral quantum devices, such as planar quantum dots³¹ and superconducting Josephson junctions^{32–34}, have been successfully fabricated. A most intriguing perspective of these layered materials is to build topological superconducting structures from them, in which Majorana fermions and parafermions^{35,36} can be created and manipulated, enabling a different route of developments towards topological quantum computation technology. A desired ingredient in constructing topological superconducting states from such a semiconductor nanostructure is strong SOI (with a few 100 nm or shorter in spin–orbit length and about 100 μ eV or larger in

spin–orbit energy) possessed in the material^{37,38}. Comprehensive studies of SOI have been carried out for InSb nanowires^{39,40} and quantum wells⁴¹. However, a desired study of SOI and, in particular, its controllability has not yet been carried out for free-standing InSb nanosheets, although it is highly anticipated that such a study would lead to great advancement in the developments of spintronics, quantum-dot based spin–orbit qubits, and topological quantum computation technology.

In this article, we report on magnetotransport measurements of an epitaxially grown, free-standing, zincblende InSb nanosheet and on employment of dual-gate technique to achieve tunable SOI in the nanosheet. Key electron transport characteristic lengths, such as the mean free path, phase coherence length, and SOI length, in the nanosheet are extracted from the measurements of the low-field magnetoconductance. We show that a strong SOI is present in the InSb nanosheet and is greatly tunable using a voltage applied over the dual gate. We also demonstrate, through band diagram simulation for the experimental structure setups, that the origin of an intrinsic SOI observed in the InSb nanosheet at zero dual-gate voltage comes from the build-in structure asymmetry in the dual-gate device. The advancement made in this work in understanding and controlling of strong SOI in the InSb nanosheet will greatly simplify the design and implementation technology for the construction of spintronic devices, spin–orbit qubits, and topological quantum devices.

RESULTS AND DISCUSSION

Dual-gate InSb nanosheet device

The dual-gate device studied in this work is made from a free-standing, single-crystalline, zincblende InSb nanosheet on an n -doped silicon (Si) substrate covered by a 300-nm-thick layer of silicon dioxide (SiO₂) on top, using standard nanofabrication techniques (see “Methods”). Figure 1a shows a scanning electron microscope (SEM) image of the device and the measurement circuit setup. Figure 1b shows a schematic view of the layer structure of the device. The InSb nanosheet in the device is

¹Beijing Key Laboratory of Quantum Devices, Key Laboratory for the Physics and Chemistry of Nanodevices and Department of Electronics, Peking University, 100871 Beijing, China. ²State Key Laboratory of Superlattices and Microstructures, Institute of Semiconductors, Chinese Academy of Sciences, P.O. Box 912, 100083 Beijing, China. ³Beijing Academy of Quantum Information Sciences, 100193 Beijing, China. ✉email: jhzhao@semi.ac.cn; hqxu@pku.edu.cn

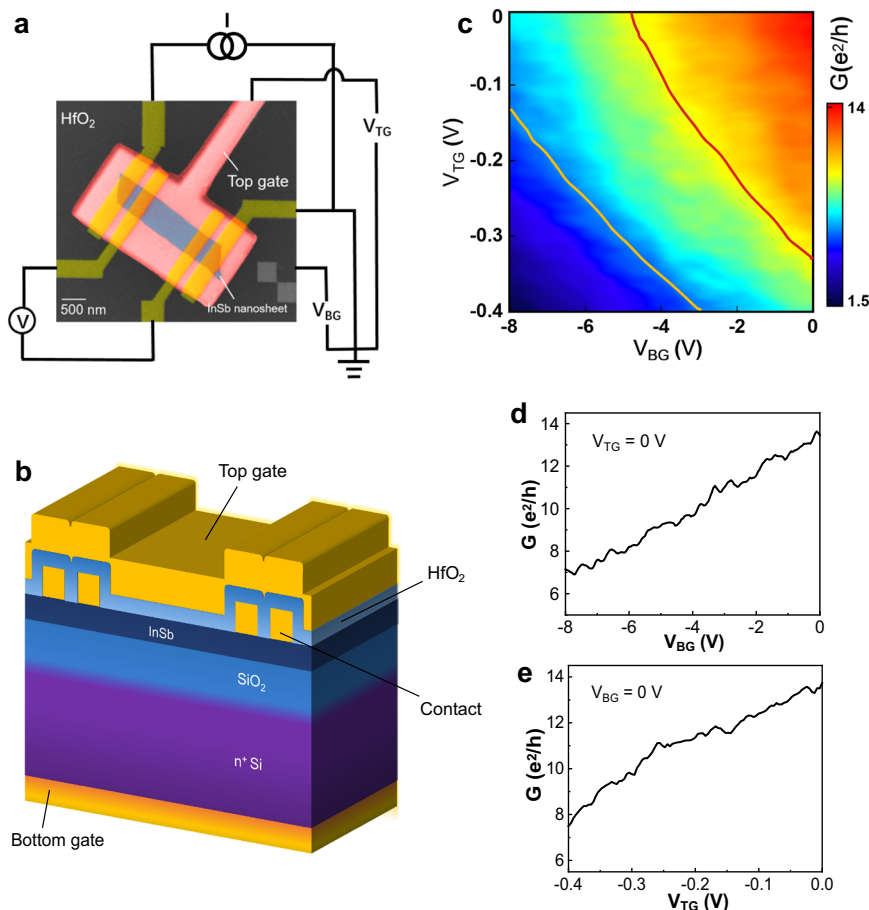


Fig. 1 Dual-gate InSb nanosheet device and its gate transfer characteristics. **a** False-colored SEM image of the device studied in this work and measurement circuit setup. The device is fabricated from an MBE-grown InSb nanosheet (transport channel) on an n-doped Si substrate (bottom gate) covered by a layer of SiO₂ on top (bottom-gate dielectric). The InSb nanosheet is contacted by four stripes of Ti/Au (contact electrodes) and is then covered by depositing a layer of HfO₂ (top-gate dielectric) and a metal bilayer of Ti/Au (top gate). The nanosheet has a width of ~550 nm and a thickness of ~30 nm. The separation between the two inner electrodes is ~1.1 μm. **b** Schematic view of the layer structure of the device. **c** Conductance G measured for the device as functions of top-gate voltage V_{TG} and bottom-gate voltage V_{BG} (gate transfer characteristics) at a temperature of $T = 1.9$ K. In the measurements, a 17-Hz AC current (I) of 100 nA is applied through the two outer electrodes, and the voltage drop (V) between the two inner electrodes is recorded and is then converted to the conductance through $G = I/V$. The red and yellow solid lines denote the constant conductance contours of ~ 9 and $\sim 5e^2/h$, respectively. **d** G as a function of bottom-gate voltage V_{BG} at $V_{TG} = 0$ V. **e** G as a function of top-gate voltage V_{TG} at $V_{BG} = 0$ V.

contacted by four stripes of Ti/Au (contact electrodes). The n-doped Si substrate (contacted by a thin gold film at the bottom) and the SiO₂ layer are employed as the bottom gate and the gate dielectric. The top gate is made from a Ti/Au film with a layer of hafnium dioxide (HfO₂) as the top-gate dielectric. The nanosheet has a width of ~550 nm and a thickness of ~30 nm (estimated based on the calibrated contrast in the SEM image). The separation between the two inner Ti/Au electrodes is 1.1 μm. Low-temperature transport measurements of the dual-gate device is carried out in a physical property measurement system (PPMS) cryostat, equipped with a uniaxial magnet, in a four-probe configuration, in which a 17-Hz AC excitation current (I) of 100 nA is supplied through the two outer electrodes and the voltage drop (V) between the two inner contact electrodes is recorded. The nanosheet channel conductance G is obtained from $G = I/V$. In measurements for the magnetoconductance, $\Delta G = G(B) - G(B = 0)$, the magnetic field is applied perpendicular to the InSb nanosheet plane.

Figure 1c shows the measured conductance of the InSb nanosheet in the device as a function of voltages, V_{BG} and V_{TG} , applied to the bottom and top gates (transfer characteristics). Figure 1d shows a horizontal line cut of Fig. 1c (bottom-gate

transfer characteristics) at $V_{BG} = 0$ V, while Fig. 1e shows a vertical line cut of Fig. 1c (top-gate transfer characteristics) at $V_{BG} = 0$ V. Conductance fluctuations superimposed on the transfer curves are observable. These fluctuations are reproducible and arise from universal conductance fluctuations⁴² (UCF). Overall, the top gate shows a strong coupling to the InSb nanosheet, while the bottom gate shows a relatively weak coupling to the nanosheet. The former is in accordance with the fact that a short distance between the top gate and the nanosheet and a high dielectric material (HfO₂ in this case) are employed in the device. From Fig. 1b, one can infer that an electric field stretching perpendicularly through the InSb nanosheet can be present and can be tuned by a voltage applied over the two gates (dual-gate voltage).

The carrier density in the InSb nanosheet can be estimated from the measured transfer characteristics. Here, we extract the carrier density, at a fixed top-gate voltage of $V_{TG} = 0$ V, from $n = C_{gs} \times \frac{V_{BG} - V_{BG}^{th}}{e}$, where e denotes the elementary charge and $C_{gs} = \frac{\epsilon \epsilon_0}{d}$ is the unit area capacitance between the bottom gate and the nanosheet with ϵ_0 being the vacuum permittivity, $\epsilon = 3.9$ the dielectric constant of SiO₂, and $d = 300$ nm the thickness of SiO₂. In the above relation, V_{BG}^{th} is the threshold voltage at which the conductance G goes to zero. In our case, to extract the

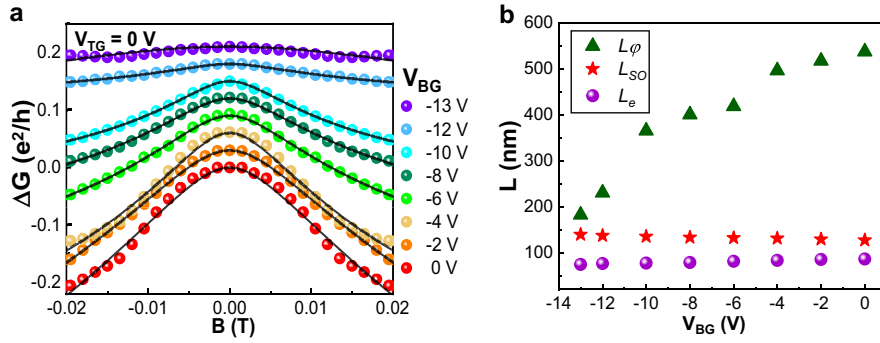


Fig. 2 Magnetotransport measurements at various bottom-gate voltages. **a** Low-field magnetoconductance, $\Delta G = G(B) - G(B = 0)$, measured for the device shown in Fig. 1a at various bottom-gate voltages V_{BG} at temperature $T = 1.9$ K. The bottom trace shows the measured magnetoconductance data at $V_{BG} = 0$ V and all other measured magnetoconductance traces are successively vertically offset for clarity. Here the top-gate voltage is set at $V_{TG} = 0$ V. The black solid lines are the theoretical fits of the experimental data to the HLN equation [Eq. (1)]. **b** Phase coherence length L_ϕ , spin-orbit length L_{SO} , and mean free path L_e , in the InSb nanosheet extracted from the fits as a function of V_{BG} .

threshold, a line fit to the measured $G - V_{BG}$ curve in Fig. 1d is made (see Supplementary Fig. 1a). Then by extending the fitting line to intersect the horizontal axis, we obtain V_{BG}^{th} . In this way, we have estimated out a carrier density of $n = 7.2 \times 10^{11} \text{ cm}^{-2}$ at $V_{BG} = -5$ V and $V_{TG} = 0$ V, at which the measured conductance takes a value of $G \sim 9e^2/h$. Note that along the red contour line in Fig. 1c, the measured conductance stays at the same value of $G \sim 9e^2/h$ and thus the carrier density in the nanosheet stays, to a good approximation, at the same value of $n = 7.2 \times 10^{11} \text{ cm}^{-2}$. Similarly, the yellow contour line in Fig. 1c displays the measurements at a conductance of $G \sim 5e^2/h$ and a carrier density of $n = 4.3 \times 10^{11} \text{ cm}^{-2}$ in the nanosheet. The electron mobility in the nanosheet is estimated from $\mu = \sigma/ne$, where $\sigma = \frac{G}{W}$ is the sheet conductivity with L being the channel length (i.e., the distance between the two inner contact electrodes, 1.1 μm in this device) and W being the channel width (i.e., the width of the nanosheet, 550 nm in this device). Since the conductance is approximately a linear function of V_{BG} and the same is for the electron density in the nanosheet, the same electron mobility of $\mu \sim 6000 \text{ cm}^2 \text{ V}^{-1} \text{ s}^{-1}$ in the nanosheet is extracted at both $G \sim 9e^2/h$ and $G \sim 5e^2/h$. The electron mean free path in the nanosheet can be estimated from $L_e = \frac{\hbar\mu}{e} \sqrt{2\pi n}$, where $\hbar = \frac{h}{2\pi}$ with h being the Planck constant, giving $L_e \sim 84$ nm at $n = 7.2 \times 10^{11} \text{ cm}^{-2}$ ($G \sim 9e^2/h$) and $L_e \sim 65$ nm at $n = 4.3 \times 10^{11} \text{ cm}^{-2}$ ($G \sim 5e^2/h$). A larger value of L_e obtained at the higher electron density could be due to screening of scattering by electrons in the nanosheet. For comparison, it is worthwhile to note that the Fermi wavelength can be estimated as $\lambda_F = \sqrt{2\pi/n} \sim 30$ nm at the carrier density of $n = 7.2 \times 10^{11} \text{ cm}^{-2}$, which is close to the thickness of the nanosheet. Thus, only one or few 2D electron subbands in the InSb nanosheet are occupied and the InSb nanosheet is dominantly a 2D electron system. The same analysis based on the top-gate transfer characteristics should give the similar estimations for the carrier density and the mobility at the same setting of V_{BG} and V_{TG} . According to this, we have extracted a value of $\epsilon \sim 6.5$ for the dielectric constant of the top-gate dielectric HfO_2 using the $G - V_{TG}$ curve shown in Fig. 1e and the carrier densities extracted through the $G - V_{BG}$ curve (see Supplementary Note 1 for detail).

Quantum transport characteristics of the InSb nanosheet

In a quantum diffusive device, the electron transport can be characterized by a set of transport length scales, including phase coherence length (L_ϕ), SOI length (L_{SO}), and mean free path (L_e). In order to determine all these lengths in the InSb nanosheet, we have performed detailed magnetotransport measurements for the dual-gate InSb nanosheet device at low magnetic fields. Figure 2a

shows the measured magnetoconductance, $\Delta G = G(B) - G(B = 0)$, at different V_{BG} with top-gate voltage set at $V_{TG} = 0$ V. Here, the magnetic field B is applied perpendicular to the nanosheet. It is seen that the measured magnetoconductance displays a peak in the vicinity of $B = 0$, i.e., the weak antilocalization (WAL) characteristics. The WAL arises from quantum interference in the presence of strong SOI and gives a positive quantum correction to the conductance at zero magnetic field. It is also seen that at $V_{BG} = 0$ V, a well-defined WAL peak is observed, but the peak becomes less pronounced as V_{BG} decreases.

For a 2D diffusive system, the low-field magnetoconductance is well described by the Hikami–Larkin–Nagaoka (HLN) quantum interference theory⁴³. Assuming that the electron transport in the InSb nanosheet is in the 2D diffusion regime, the quantum correction to the low-field magnetoconductance is given by

$$\Delta G(B) = -\frac{e^2}{\pi h} \left[\frac{1}{2} \Psi \left(\frac{B_\phi}{B} + \frac{1}{2} \right) + \Psi \left(\frac{B_e}{B} + \frac{1}{2} \right) - \frac{3}{2} \Psi \left(\frac{(4/3)B_{SO} + B_\phi}{B} + \frac{1}{2} \right) - \frac{1}{2} \ln \left(\frac{B_\phi}{B} \right) - \ln \left(\frac{B_e}{B} \right) + \frac{3}{2} \ln \left(\frac{(4/3)B_{SO} + B_\phi}{B} \right) \right]. \quad (1)$$

Here, $\Psi(x)$ is the digamma function. Three subscripts, ϕ , SO, and e , in the above equation denote inelastic dephasing, spin-orbit scattering, and elastic scattering processes, respectively. $B_{\phi,SO,e}$ are the characteristic fields for the three scattering mechanisms and are given by $B_{\phi,SO,e} = \hbar/(4eL_{\phi,SO,e}^2)$. The measured low-field magnetoconductance data at different V_{BG} shown in Fig. 2a are fitted to Eq. (1) using L_ϕ , L_{SO} , and L_e as fitting parameters (see further detail in “Methods”). The black solid lines in Fig. 2a are the results of the fits.

Figure 2b shows the extracted L_ϕ , L_{SO} , and L_e in the InSb nanosheet from the fits at $V_{TG} = 0$ V as a function of V_{BG} . As shown in Fig. 2b, L_ϕ is strongly dependent on V_{BG} , while L_{SO} and L_e show weak V_{BG} dependences and stay at values of $L_{SO} \sim 130$ nm and $L_e \sim 80$ nm. Here, we note that the extracted $L_e \sim 80$ nm is in good agreement with the values extracted above from the gate transfer characteristics. The weak V_{BG} dependence of L_e arises from the fact that at the low temperature we have considered, L_e is primarily given by the distribution of scattering carriers, such as charged impurities and lattice defects, in the conduction InSb channel and the dielectric SiO_2 layer, as well as at the InSb– SiO_2 interface, and the distribution of scattering centers should be insensitive to a change in the gate voltage in the range we have considered. The L_{SO} also shows a weak V_{BG} dependence because it primarily depends on the perpendicular electric field penetrated through the InSb nanosheet, which is only weakly dependent on V_{BG} when the InSb nanosheet is at open conduction state. At $V_{BG} = 0$ V (a high carrier density case), the extracted L_ϕ reaches to ~ 530 nm.

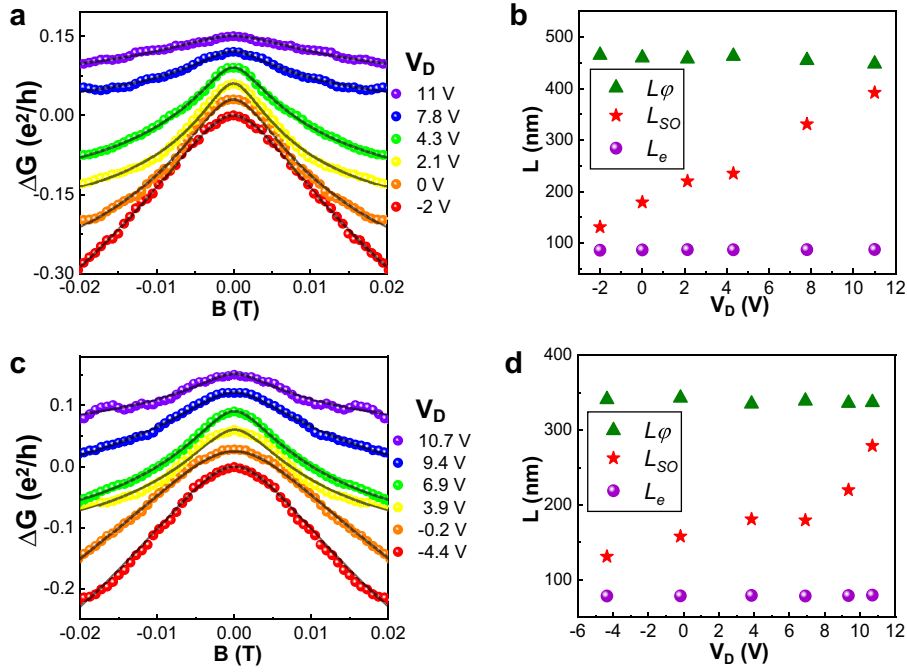


Fig. 3 Magnetotransport measurements at various voltages applied over the dual gate at constant carrier densities in the InSb nanosheet. **a** Low-field magnetoconductance ΔG measured for the device at a constant conductance of $\sim 9e^2/h$ and temperature $T = 1.9$ K at various values of dual-gate voltage $V_D = V_{TG} - V_{BG}$. The bottom trace shows the measured magnetoconductance data at $V_D = -2$ V and all other measured magnetoconductance traces are successively vertically offset for clarity. The black solid lines are the theoretical fits of the experimental data to the HLN equation [Eq. (1)]. **b** Phase coherence length L_ϕ , spin-orbit length L_{SO} , and mean free path L_e extracted from the fits in **a** as a function of V_D . **c** The same as **a** but measured for the device at a constant conductance of $\sim 5e^2/h$. Here, the bottom trace shows the measured magnetoconductance data at $V_D = -4.4$ V and all other measured magnetoconductance traces are again successively vertically offset for clarity. **d** Phase coherence length L_ϕ , spin-orbit length L_{SO} , and mean free path L_e extracted from the fits in **c** as a function of V_D .

As V_{BG} sweeps from 0 to -13 V, L_ϕ decreases rapidly to ~ 180 nm, indicating that the dephasing is stronger at a lower carrier density. The physical origin of this increase in L_ϕ with increasing carrier density is that, at this low temperature, the dephasing arises predominantly from electron-electron interaction with small energy transfers, in the form of electromagnetic field fluctuations generated by the motions of neighboring electrons (the Nyquist dephasing mechanism⁴⁴), and such fluctuations get to be diminished at a higher carrier density and thus an increased bottom-gate voltage due to stronger charge screening. It is worthwhile to emphasize that L_ϕ is one order of magnitude larger than the thickness of the nanosheet. This, together with the fact that the typical Fermi wavelength $\lambda_F \sim 30$ nm is close to the thickness of the nanosheet, supports our assumption that the transport in the nanosheet is of a 2D nature. In addition, the extracted $L_e \sim 80$ nm is one order of magnitude smaller than the distance between the two inner contact electrodes, indicating that the transport in the nanosheet is in the diffusion regime.

There are several possible mechanisms responsible for the spin relaxation process in the nanosheet. One is the Elliot-Yafet mechanism^{45,46}, i.e., the spin randomization due to momentum scattering. In the Elliot-Yafet mechanism, the spin relaxation length can be estimated out as^{39,47}

$$L_{SO,EY} = \sqrt{\frac{3}{8}} \cdot \frac{E_G}{E_F} \cdot L_e \cdot \frac{(E_G + \Delta_{SO})(3E_G + 2\Delta_{SO})}{\Delta_{SO}(2E_G + \Delta_{SO})} \geq 500 \text{ nm},$$

using the bandgap $E_G = 0.23$ eV, the Fermi energy $E_F = \frac{\hbar^2 \pi n}{m^*} \leq 50$ meV (with $n \leq 7.2 \times 10^{11} \text{ cm}^{-2}$), bulk spin-orbit gap⁴⁸ $\Delta_{SO} \sim 0.8$ eV, and the mean free path $L_e \sim 80$ nm. The estimated $L_{SO,EY}$ is much larger than the experimentally extracted value of $L_{SO} \sim 130$ nm. Therefore, the Elliot-Yafet mechanism does not play a key role in our system. Another one is the D'yakonov-Perel' mechanism⁴⁹, which considers the spin precession between

scattering events. Since the InSb nanosheets used in our device is a zincblende crystal and the current flow would take along a $\langle 111 \rangle$ or a $\langle 110 \rangle$ crystallographic direction²⁷, the Dresselhaus SOI⁵⁰ would be either absent or negligible⁵¹. Based on the above analyses, we expect that the Rashba SOI⁵² is the primary cause of spin relaxation in the InSb nanosheet. This expectation is also consistent with our designed device structure with an enhanced structural asymmetry. Hence we can obtain a Rashba spin-orbit strength of $a_R \sim 0.42$ eV Å according to $L_{SO} = \hbar^2/m^* a_R$, where $m^* = 0.014 m_0$ denotes the effective mass of electrons in InSb with m_0 being the free electron mass. The spin-orbit energy can be determined as $E_{SO} = \frac{m^* a_R^2}{2\hbar^2} \sim 160$ μeV in the InSb nanosheet. In comparison with most commonly employed III-V narrow bandgap semiconductor nanostructures with a strong SOI, the extracted spin-orbit strength of $a_R \sim 0.42$ eV Å in our InSb nanosheet from the low-field magnetotransport measurements shown in Fig. 3 is smaller than but comparable to the values of 0.5–1 eV Å found in InSb nanowires³⁹, but is significantly larger than the values of ~ 0.16 eV Å found in InAs nanowires⁵³. In addition, our extracted spin-orbit strength in the InSb nanosheet is an order of magnitude larger than the values reported previously for InSb and InAs quantum wells^{41,54}. Thus, the extracted $a_R \sim 0.42$ eV Å in our InSb nanosheet corresponds to a strong SOI found in a III-V narrow bandgap semiconductor nanostructure.

Tuning the SOI in the InSb nanosheet by dual-gate voltage

The SOI of the Rashba type is tunable by applying an electric field perpendicularly through the InSb nanosheet. Such an electric field can be achieved and tuned by a voltage V_D applied over the dual

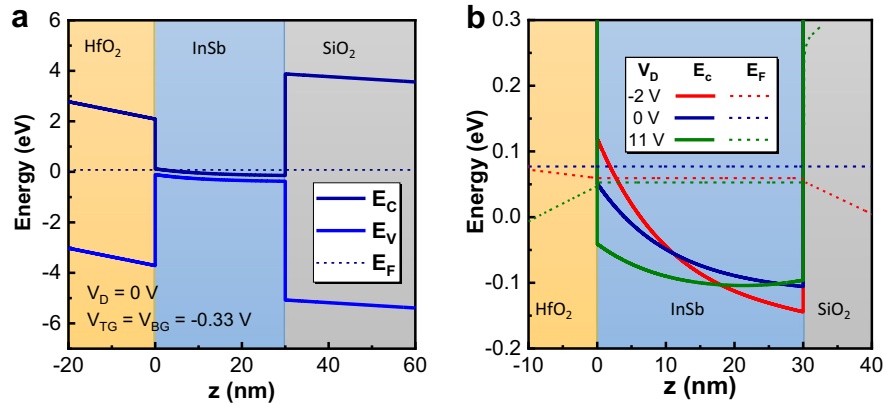


Fig. 4 Simulated band diagrams. **a** Simulated energy band diagram of the HfO₂–InSb–SiO₂ structure in the device at $V_D = 0$ V (with $V_{BG} = V_{TG} = -0.33$ V). The conduction and valence band edges E_c and E_v , are marked by the dark blue and light blue solid lines, while the Fermi level E_F is marked by the dark blue dashed line. **b** Zoom-in plots (red, blue, and green solid lines) showing the details of the conduction band edges inside the InSb nanosheet at three different values of V_D . The red, blue, and green dashed lines mark the Fermi levels obtained in the simulations at the three different values of V_D .

gate. For example, with V_{TG} being set at 0 V, we could sweep V_{BG} to gradually change V_D and thus the electric field through the nanosheet. However, as we showed above, sweeping V_{BG} only also tunes the carrier density in the nanosheet. To demonstrate the manipulation of SOI solely via the vertical electric field in the nanosheet, the carrier density in the nanosheet ought to be fixed. In the present work, this is achieved by performing magnetotransport measurements along an equal conductance contour line, in which the carrier density in the nanosheet approximately stays at a constant value, but the dual-gate voltage, $V_D = V_{TG} - V_{BG}$, is tuned continuously. Figure 3a shows magnetoconductance traces measured along a contour line of $G \sim 9e^2/h$ (the red contour line in Fig. 1c) at several values of V_D . It is seen that all the measured magnetoconductance traces show the WAL characteristics. To extract the transport length scales as a function of V_D , we fit these measured magnetoconductance traces to Eq. (1). The black solid lines in Fig. 3a show the results of the fits. Figure 3b displays the characteristic transport lengths L_ϕ , L_{SO} , and L_e extracted from the fits. It is shown that L_ϕ stays at a constant value of ~ 460 nm, independent of V_D . This is in good agreement with the fact that L_ϕ is mainly influenced by carrier density and temperature, but not by an electric field applied perpendicular to the nanosheet. The same is also true for L_e , which is found to stay at a value of ~ 85 nm. However, L_{SO} shows a strong dependence on V_D . As seen in Fig. 3b, L_{SO} is monotonically increased from ~ 130 to ~ 390 nm as V_D changes from -2 to 11 V, indicating that the SOI strength becomes weaker as V_D moves towards more positive values. Figure 3c shows the magnetoconductance traces measured along a constant conductance contour line of $G \sim 5e^2/h$ (the yellow contour line in Fig. 1c) at varying V_D from -4.4 to 10.7 V. Again, the WAL characteristics are observed in the measurements. The black solid lines in Fig. 3c show the fits of the measurements to Eq. (1) and Fig. 3d shows the transport lengths extracted from the fits. Again, it is seen that with varying V_D , L_ϕ stays at a value of ~ 340 nm and L_e stays at a value of ~ 78 nm. i.e., both are independent of V_D . However, L_{SO} is seen to increase from ~ 130 to ~ 270 nm as V_D is tuned from -4.4 to 10.7 V. Our results presented in Fig. 3 clearly demonstrate that the SOI in the InSb nanosheet of our dual-gate device can be effectively tuned by applying a voltage over the dual gate without a change in the carrier density in the nanosheet. The achieved change in L_{SO} from 130 to 390 nm corresponds to a change in the spin–orbit strength from 0.42 to 0.14 eVÅ and a change in the spin–orbit energy from 160 to 18 μ eV.

We have also performed the dual-gate voltage V_D dependent measurements of the transport characteristics lengths L_ϕ , L_{SO} , and

L_e in the InSb nanosheet along the constant conductance contour lines of ~ 2.6 and $\sim 1.1e^2/h$, and an efficient tuning of SOI in the nanosheet by the dual-gate voltage V_D is again observed (see Supplementary Note V). All the results presented in the present section (and in Supplementary Fig. 5) manifest that the SOI in the InSb nanosheet in a dual-gate structure can be efficiently tuned by a voltage applied to the dual gate at largely different but fixed carrier densities of the nanosheet.

Band diagram and intrinsic Rashba SOI in the InSb nanosheet

It is important to emphasize that the experimentally extracted Rashba spin–orbit length L_{SO} is small, indicating a strong SOI, even at $V_D = 0$ V. This seemingly unexpected observation however reveals the presence of an intrinsic structural asymmetry even in the absence of a voltage difference between the top and bottom gates due to band offsets appeared in the HfO₂–InSb–SiO₂ heterostructure. To show this, the energy band diagram in the vertical direction is simulated using commercially available software COMSOL. The simulation is mainly based on Poisson’s equations and takes the material parameters of HfO₂, InSb, and SiO₂, including bandgaps, dielectric constants, electron effective masses, and electron affinities, as inputs (see Supplementary Table 1 for material parameters). Figure 4a displays the simulated energy band diagram of the HfO₂–InSb–SiO₂ structure at $V_D = 0$ V (with $V_{TG} = V_{BG} = -0.33$ V) and carrier density $n = 7.2 \times 10^{11} \text{ cm}^{-2}$ in the InSb nanolayer. The conduction band and the valence band edges exhibit a noticeable bending even at $V_D = 0$ V, illustrating the presence of an intrinsic structure asymmetry in the InSb nanosheet. Figure 4b shows a zoom-in view of the simulated conduction band edge in the InSb nanosheet at three values of V_D . The green, blue, and red solid lines represent the conduction band edges at $V_D = 0$, -2 (with $V_{TG} = -0.46$ V and $V_{BG} = 1.54$ V), and 11 V ($V_{TG} = 0.4$ V and $V_{BG} = -10.6$ V), respectively, and the carrier density of $n = 7.2 \times 10^{11} \text{ cm}^{-2}$ in the InSb nanosheet. With pushing the dual-gate voltage from $V_D = 0$ V to $V_D = -2$ V, we can see that the band bending becomes stronger, indicating an enhanced structural asymmetry and thus a stronger Rashba SOI. On the contrary, by moving from $V_D = 0$ V to $V_D = 11$ V, we compensate the band bending towards a nearly flat band, leading to a reduced asymmetry in the structure and a weaker Rashba SOI. These simulated results are fully in line with the experimental observations. Based on the simulations, the strength of the vertical, effective mean electric field in the InSb nanosheet can be estimated. It is found that the field strength gradually increases when changing from $V_D = 11$ V to $V_D = -2$ V (see Supplementary

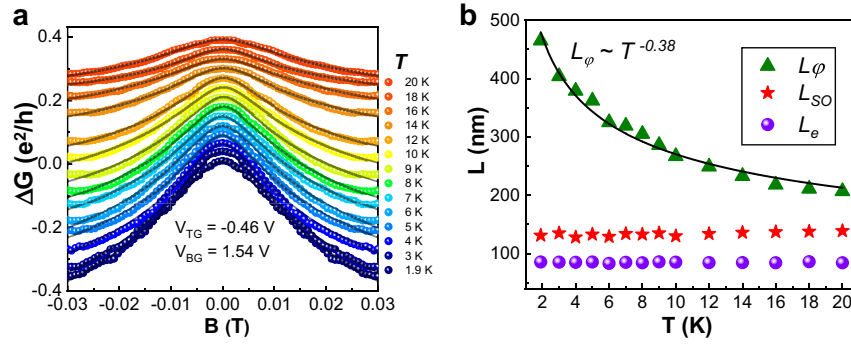


Fig. 5 Temperature-dependent magnetotransport measurements. **a** Low-field magnetoconductance ΔG measured for the device at $V_{BG} = 1.54$ V and $V_{TG} = -0.46$ V, corresponding to a conductance value of $\sim 9e^2/h$ and a dual-gate voltage value of $V_D = -2$ V, at different temperatures T . The bottom trace shows the measured magnetoconductance data at $T = 1.9$ K and all other measured magnetoconductance traces are successively vertically offset for clarity. **b** Phase coherence length L_ϕ , spin-orbit length L_{SO} , and mean free path L_e extracted by fitting the measured data to Eq. (1) as a function of temperature T . The black solid line is a power-law fit to the extracted phase coherence length L_ϕ showing $L_\phi \sim T^{-0.38}$.

Fig. 3), providing a numerical evidence for tunable structural asymmetry and thus tunable SOI in the nanosheet. Furthermore, the material-specific, Fermi-level-dependent Rashba prefactor r_R , defined via the Rashba coefficient $\alpha_R = r_R E$ with E being the strength of the perpendicular electric field in the InSb nanosheet⁴⁸, can be determined (see Supplementary Note IV for details). The Rashba prefactors extracted for the InSb nanosheet are $r_R = 4.26e$ nm² at carrier density $n = 7.2 \times 10^{11}$ cm⁻² and $r_R = 3.48e$ nm² at carrier density $n = 4.3 \times 10^{11}$ cm⁻².

Temperature effects

Figure 5a shows the measured low-field magnetoconductance of the device at $V_{BG} = 1.54$ V and $V_{TG} = -0.46$ V at temperatures of 1.9 to 20 K. At temperature $T = 1.9$ K, a sharp WAL peak is seen in the vicinity of zero magnetic field. As the temperature increases, both the height of the WAL peak and the fluctuation magnitude of the UCF patterns become gradually suppressed, although they still remain visible at $T = 20$ K. Again, we fit these measured magnetoconductance data to Eq. (1) and plot the results in black solid lines in Fig. 5a. Extracted L_ϕ , L_{SO} , and L_e from the fits are displayed in Fig. 5b. It can be found that both L_{SO} and L_e are weakly dependent on temperature, while L_ϕ shows a strong temperature dependence, decreasing rapidly from ~ 470 to ~ 210 nm with increasing temperature from 1.9 to 20 K. The temperature dependence of L_ϕ is found to follow a power law of $L_\phi \sim T^{-0.38}$ (see the solid line in Fig. 5b). The power index of -0.38 falls between the values of $-1/2$ and $-1/3$, corresponding to the Nyquist dephasing processes⁴⁴ in a 2D ($T^{-1/2}$) and a 1D system ($T^{-1/3}$). Since L_ϕ is in the same order of length scale as the width of the conduction channel (~ 550 nm), the transport in the InSb nanosheet is more likely in an intermediate regime between the 1D and 2D limits⁵⁵.

In summary, a dual-gate planar device made from a single-crystalline zincblende InSb nanosheet is fabricated and the quantum transport properties of the InSb nanosheet in the device are studied by low-field magnetotransport measurements. Carrier density, mean free path, coherence length, and SOI strength in the InSb nanosheet are extracted. It is shown that the measured low-field magnetoconductance can be excellently described by the 2D diffusive HLN quantum transport theory and exhibits the WAL characteristics. The origin of the WAL characteristics is identified as the presence of strong SOI of the Rashba type in the InSb nanosheet. By performing the magnetoconductance measurements of the InSb nanosheet at constant carrier densities, we demonstrate that the Rashba SOI strength can be efficiently tuned by a voltage applied over the dual gate. We also observe the presence of a strong SOI in the InSb nanosheet at zero dual-gate

voltage. By simulations for the band diagrams of the device structure, we identify the origin of this intrinsic SOI in the InSb nanosheet as the presence of band bending in the nanosheet even at zero dual-gate voltage. The strong and tunable Rashba SOI in the InSb nanosheet, demonstrated in this work, lays the groundwork for employing this emerging layered material in the developments of spintronics, spin qubits, and topological quantum devices.

METHODS

Material growth

High-quality, free-standing, single-crystalline, pure zincblende phase InSb nanosheets used in this work are grown by molecular-beam epitaxy (MBE) on top of InAs nanowires on a Si (111) substrate. The growth process starts by depositing a thin layer of Ag on the Si substrate in an MBE chamber. The film is subsequently annealed in situ to form Ag nanoparticles. Thin InAs nanowires are then grown with these Ag nanoparticles as seeds. The InSb nanosheets are grown on top of the InAs nanowires by abruptly switching the group-V source from As to Sb and with an increased Sb flux. High-resolution transmission electron microscopy and scanning electron microscopy analyses show that the as-grown InSb nanosheets are of high-quality, pure zincblende phase, single crystals and are up to several micrometers in sizes and down to ~ 10 nm in thickness. For further details about the growth process and structural properties of our MBE-grown InSb nanosheets, we refer to ref. 27.

Device fabrication

For device fabrications, the MBE-grown InSb nanosheets are mechanically transferred from the growth substrate onto an n-doped Si substrate covered with a 300-nm-thick layer of SiO₂ on top. The Si and SiO₂ layers are later used as a global bottom gate and its dielectric. After transferring, contact electrodes are fabricated on selected nanosheets with a thickness of $t \sim 30$ nm via a combined process of electron-beam lithography (EBL), electron-beam evaporation (EBE) of a Ti/Au (5/90 nm in thickness) metal bilayer, and lift off. We note that before the metal evaporation, the exposed areas on the InSb nanosheets are chemically etched in a de-ionized water-diluted (NH₄)₂S_x solution to remove the surface oxide and to subsequently passivate the fresh surface. After the contact electrode fabrication, a 20-nm-thick HfO₂ dielectric layer is deposited on the sample by atomic layer deposition. Finally, a Ti/Au (5/90 nm in thickness) metal bilayer top gate is fabricated on each device by the combined process of EBL, EBE and lift off, again. Figure 1a shows a false-colored SEM image of a fabricated device measured for this work and the measurement circuit setup. In this device, four parallel contact electrodes are made on the InSb nanosheet and the distance between the two inner contact electrodes is ~ 1.1 μ m. The top gate covers the entire InSb nanosheet as seen in Fig. 1a and as indicated in the schematic shown in Fig. 1b.

Gate transfer characteristics and magnetotransport measurements

Low-temperature transport measurements of the fabricated devices are carried out in a PPMS cryostat equipped with a uniaxial magnet. The InSb nanosheet conductance is measured in a four-probe configuration to eliminate the impact of the contact resistances using a lock-in technique, in which a 17-Hz AC excitation current I of 100 nA is supplied between the two outer electrodes and the voltage drop V between the two inner contact electrodes is recorded. The nanosheet channel conductance G is obtained numerically from $G = I/V$. For this work, the results of the measurements obtained from a representative device as shown in Fig. 1a are presented. The measurements are carried out with magnetic fields applied perpendicular to the nanosheet plane at temperatures of $T = 1.9\text{--}20$ K.

Fitting of the measured magnetoconductance data to the HLN formula

To extract the characteristic transport lengths of L_{ϕ} , L_{SO} , and L_e in the InSb nanosheet, the measured data are fitted to Eq. (1), based on the least-squares method, using both the “curve_fit” function in the SciPy package written in Python and the non-linear fit program in the Origin software for crosscheck. The two fitting procedures give almost the same results. The fitting bounds are set in order to make the corresponding length scales vary in a reasonable range. For example, we set the fitting bound of L_e as $L_e \leq 200$ nm. The range of magnetic fields B is chosen to be $|B| \leq 20$ mT in all the fittings presented in this work in order to make the low-field condition of Eq. (1) satisfied.

Band diagram simulation

To simulate the energy band diagrams of the $\text{HfO}_2\text{-InSb-SiO}_2$ heterostructure in the device, Poisson's equations are solved using commercially available program COMSOL in compliance with the boundary conditions of the system. An effective one-dimensional model with three sections representing three different materials, HfO_2 , InSb, and SiO_2 , is considered. Material properties employed in the simulation, include bandgaps, dielectric constants, electron effective masses, and electron affinities, are listed in Supplementary Table I. The carrier density in the InSb nanosheet and the boundary conditions used in the simulation are acquired from the experiments. We first show the different degrees of band bending, i.e., the different degrees of asymmetry, when various voltages are applied to the top and bottom gates (Fig. 4 and Supplementary Fig. 3a). The carrier density distribution inside the InSb layer can also be calculated (see Supplementary Fig. 3c). It is seen that the carrier density is non-uniformly distributed, consistent with the conduction band bending profile obtained. The quantitative analysis of the asymmetry is carried out from the calculated effective electric field strength inside the InSb layer shown in Supplementary Fig. 3b.

DATA AVAILABILITY

The data supporting the findings of this study are available within the article and its Supplementary Information file. Additional data including simulation codes are available from the corresponding author upon reasonable request.

Received: 6 July 2020; Accepted: 18 November 2020;

Published online: 04 January 2021

REFERENCES

- Ahish, S., Sharma, D., Vasantha, M. H., & Kumar, Y. B. N. Design and analysis of novel InSb/Si heterojunction double gate tunnel field effect transistor. In *IEEE Computer Society Annual Symposium on VLSI (ISVLSI)*, Pittsburgh, PA, USA, 105–109 (2016).
- Chochol, J., Postava, K., Čada, M. & Pištora, J. Experimental demonstration of magnetoplasmon polariton in InSb(InAs)/dielectric interface for terahertz sensor application. *Sci. Rep.* **7**, 1–8 (2017).
- Yang, Z. et al. Spin transport in ferromagnet-InSb nanowire quantum devices. *Nano Lett.* **20**, 3232–3239 (2020).
- Nowack, K. C., Koppens, F. H. L., Nazarov, Yu. V. & Vandersypen, L. M. K. Coherent control of a single electron spin with electric fields. *Science* **318**, 1430–1433 (2007).

- Van den Berg, J. W. G. et al. Fast spin-orbit qubit in an indium antimonide nanowire. *Phys. Rev. Lett.* **110**, 066806 (2013).
- Nayak, C., Simon, S. H., Stern, A., Freedman, M. & Sarma, S. D. Non-Abelian anyons and topological quantum computation. *Rev. Mod. Phys.* **80**, 1083 (2008).
- Gül, Ö. et al. Towards high mobility InSb nanowire devices. *Nanotechnology* **26**, 215202 (2015).
- Fan, D., Kang, N., Ghalamestani, S. G., Dick, K. A. & Xu, H. Q. Schottky barrier and contact resistance of InSb nanowire field-effect transistors. *Nanotechnology* **27**, 275204 (2016).
- Nilsson, H. A. et al. Giant, level-dependent g factors in InSb nanowire quantum dots. *Nano Lett.* **9**, 3151–3156 (2009).
- Nilsson, H. A. et al. Correlation-induced conductance suppression at level degeneracy in a quantum dot. *Phys. Rev. Lett.* **104**, 186804 (2010).
- Fan, D. et al. Formation of long single quantum dots in high quality InSb nanowires grown by molecular beam epitaxy. *Nanoscale* **7**, 14822–14828 (2015).
- Nadj-Perge, S. et al. Spectroscopy of spin-orbit quantum bits in indium antimonide nanowires. *Phys. Rev. Lett.* **108**, 166801 (2012).
- Pribiag, V. S. et al. Electrical control of single hole spins in nanowire quantum dots. *Nat. Nanotechnol.* **8**, 170–174 (2013).
- Mourik, V. et al. Signatures of Majorana fermions in hybrid superconductor-semiconductor nanowire devices. *Science* **336**, 1003–1007 (2012).
- Deng, M. T. et al. Anomalous zero-bias conductance peak in a Nb-InSb nanowire-Nb hybrid device. *Nano Lett.* **12**, 6414–6419 (2012).
- Gül, Ö. et al. Hard superconducting gap in InSb nanowires. *Nano Lett.* **17**, 2690–2696 (2017).
- Li, S., Kang, N., Caroff, P. & Xu, H. Q. $0-\pi$ phase transition in hybrid superconductor-InSb nanowire quantum dot devices. *Phys. Rev. B* **95**, 014515 (2017).
- Kitaev, A. Y. Unpaired Majorana fermions in quantum wires. *Phys. Usp.* **44**, 131–136 (2001).
- Alicea, J. New directions in the pursuit of Majorana fermions in solid state systems. *Rep. Prog. Phys.* **75**, 076501 (2012).
- Sau, J. D., Clarke, D. J. & Tewari, S. Controlling non-Abelian statistics of Majorana fermions in semiconductor nanowires. *Phys. Rev. B* **84**, 094505 (2011).
- Van Heck, B., Akhmerov, A. R., Hassler, F., Burrello, M. & Beenakker, C. W. J. Coulomb-assisted braiding of Majorana fermions in a Josephson junction array. *N. J. Phys.* **14**, 035019 (2012).
- Teo, J. C. & Kane, C. L. Majorana fermions and non-Abelian statistics in three dimensions. *Phys. Rev. Lett.* **104**, 046401 (2010).
- Aasen, D. et al. Milestones toward Majorana-based quantum computing. *Phys. Rev. X* **6**, 031016 (2016).
- Hell, M., Leijnse, M. & Flensberg, K. Two-dimensional platform for networks of Majorana bound states. *Phys. Rev. Lett.* **118**, 107701 (2017).
- Ke, C. T. et al. Ballistic superconductivity and tunable π -junctions in InSb quantum wells. *Nat. Commun.* **10**, 1–6 (2019).
- Lei, Z. et al. Quantum transport in high-quality shallow InSb quantum wells. *Appl. Phys. Lett.* **115**, 012101 (2019).
- Pan, D. et al. Free-standing two-dimensional single-crystalline InSb nanosheets. *Nano Lett.* **16**, 834–841 (2016).
- De La Mata, M. et al. Twin-induced InSb nanosails: a convenient high mobility quantum system. *Nano Lett.* **16**, 825–833 (2016).
- Gazibegovic, S. et al. Bottom-up grown 2D InSb nanostructures. *Adv. Mater.* **31**, 1808181 (2019).
- Kang, N. et al. Two-dimensional quantum transport in free-standing InSb nanosheets. *Nano Lett.* **19**, 561–569 (2018).
- Xue, J. et al. Gate defined quantum dot realized in a single crystalline InSb nanosheet. *Appl. Phys. Lett.* **114**, 023108 (2019).
- Zhi, J. et al. Supercurrent and multiple Andreev reflections in InSb nanosheet SNS junctions. *Phys. Status Solidi B* **256**, 1800538 (2019).
- Zhi, J. et al. Coexistence of induced superconductivity and quantum Hall states in InSb nanosheets. *Phys. Rev. B* **99**, 245302 (2019).
- de Vries, F. K. et al. Crossed Andreev reflection in InSb flake Josephson junctions. *Phys. Rev. Res.* **1**, 032031 (2019).
- Read, N. & Rezayi, E. Beyond paired quantum Hall states: parafermions and incompressible states in the first excited Landau level. *Phys. Rev. B* **59**, 8084 (1999).
- Hutter, A. & Loss, D. Quantum computing with parafermions. *Phys. Rev. B* **93**, 125105 (2016).
- Sau, J. D., Tewari, S. & Sarma, S. D. Experimental and materials considerations for the topological superconducting state in electron- and hole-doped semiconductors: searching for non-Abelian Majorana modes in 1D nanowires and 2D heterostructures. *Phys. Rev. B* **85**, 064512 (2012).
- Stanescu, T. D., Lutchyn, R. M. & Sarma, S. D. Majorana fermions in semiconductor nanowires. *Phys. Rev. B* **84**, 144522 (2011).

39. Van Weperen, I. et al. Spin-orbit interaction in InSb nanowires. *Phys. Rev. B* **91**, 201413 (2015).
40. Kallaher, R. L., Heremans, J. J., Goel, N., Chung, S. J. & Santos, M. B. Spin and phase coherence lengths in n-InSb quasi-one-dimensional wires. *Phys. Rev. B* **81**, 035335 (2010).
41. Kallaher, R. L., Heremans, J. J., Goel, N., Chung, S. J. & Santos, M. B. Spin-orbit interaction determined by antilocalization in an InSb quantum well. *Phys. Rev. B* **81**, 075303 (2010).
42. Lee, P. A. & Stone, A. D. Universal conductance fluctuations in metals. *Phys. Rev. Lett.* **55**, 1622 (1985).
43. Hikami, S., Larkin, A. I. & Nagaoka, Y. Spin-orbit interaction and magnetoresistance in the two dimensional random system. *Prog. Theor. Phys.* **63**, 707–710 (1980).
44. Altshuler, B. L., Aronov, A. G. & Khmel'nitsky, D. E. Effects of electron-electron collisions with small energy transfers on quantum localisation. *J. Phys. C* **15**, 7367–7386 (1982).
45. Yafet, Y. *Solid State Physics* Vol. 14 (eds. Seitz, F. & Turnbull D.) (Academic Press, 1963).
46. Elliot, R. J. Theory of the effect of spin-orbit coupling on magnetic resonance in some semiconductors. *Phys. Rev.* **96**, 266–279 (1954).
47. Chazalviel, J. Spin relaxation of conduction electrons in n-type indium antimonide at low temperature. *Phys. Rev. B* **11**, 1555 (1975).
48. Winkler, R. *Spin-Orbit Coupling Effects in Two-Dimensional Electron and Hole Systems* (Springer Tracts in Modern Physics) Vol. 191 (Springer, 2003).
49. D'yakonov, M. I. & Perel', V. I. Spin relaxation of conduction electrons in non-centrosymmetric semiconductors. *Sov. Phys. Solid State* **13**, 3023–3026 (1972).
50. Dresselhaus, G. Spin-orbit coupling effects in zinc blende structures. *Phys. Rev.* **100**, 580 (1955).
51. Fabian, J., Matos-Abiague, A., Ertler, C., Stano, P. & Zutic, I. Semiconductor spintronics. *Acta Phys. Slov.* **57**, 565–907 (2007).
52. Bychkov, Y. A. & Rashba, E. Oscillatory effects and the magnetic susceptibility of carriers in inversion layers. *J. Phys. C* **17**, 6039–6045 (1984).
53. Hansen, A., Björk, M., Fasth, C., Thelander, C. & Samuelson, L. Spin relaxation in InAs nanowires studied by tunable weak antilocalization. *Phys. Rev. B* **71**, 205328 (2005).
54. Heida, J. P., van Wees, B. J., Kuipers, J. J., Klapwijk, T. M. & Borghs, G. Spin-orbit interaction in a two-dimensional electron gas in a InAs/AlSb quantum well with gate-controlled electron density. *Phys. Rev. B* **57**, 11911 (1998).
55. Ando, T., Fowler, A. B. & Stern, F. Electronic properties of two-dimensional systems. *Rev. Mod. Phys.* **54**, 437–672 (1982).

ACKNOWLEDGEMENTS

This work is supported by the Ministry of Science and Technology of China through the National Key Research and Development Program of China (Grant Nos. 2017YFA0303304, 2016YFA0300601, 2017YFA0204901, and 2016YFA0300802), the National Natural Science Foundation of China (Grant Nos. 11874071, 91221202, 91421303, 11274021, and 61974138), and the Beijing Academy of Quantum

Information Sciences (Grant No. Y18G22). D.P. also acknowledges the support from the Youth Innovation Promotion Association of the Chinese Academy of Sciences (No. 2017156).

AUTHOR CONTRIBUTIONS

H.Q.X. conceived and supervised the project. Y.C. and S.H. fabricated the devices and carried out the transport measurements. D.P. and J.Z. grew the materials. J.X. and L.Z. participated in the device fabrication and measurements. Y.C. performed the band diagram simulations. Y.C., S.H., and H.Q.X. analyzed the data and wrote the manuscript with contributions from all authors. All authors contributed to the discussion of the results and the interpretation of the data acquired.

COMPETING INTERESTS

The authors declare no competing interests.

ADDITIONAL INFORMATION

Supplementary information is available for this paper at <https://doi.org/10.1038/s41699-020-00184-y>.

Correspondence and requests for materials should be addressed to J.Z. or H.Q.X.

Reprints and permission information is available at <http://www.nature.com/reprints>

Publisher's note Springer Nature remains neutral with regard to jurisdictional claims in published maps and institutional affiliations.



Open Access This article is licensed under a Creative Commons Attribution 4.0 International License, which permits use, sharing, adaptation, distribution and reproduction in any medium or format, as long as you give appropriate credit to the original author(s) and the source, provide a link to the Creative Commons license, and indicate if changes were made. The images or other third party material in this article are included in the article's Creative Commons license, unless indicated otherwise in a credit line to the material. If material is not included in the article's Creative Commons license and your intended use is not permitted by statutory regulation or exceeds the permitted use, you will need to obtain permission directly from the copyright holder. To view a copy of this license, visit <http://creativecommons.org/licenses/by/4.0/>.

© The Author(s) 2021